Polymer diffusive instability of viscoelastic Poiseuille flow between slippery walls

Bin Zhang ,[1,2] Yuke Li ,[3,4] Hongna Zhang,[5] Guiren Wang,[6] Rong Liu,[7] Shaowei Wang ,[8,*] and Zijing Ding [2,9,†]

[1]*School of Energy Science and Engineering, Harbin Institute of Technology, Harbin 150001, China*
[2]*International Research Center for Intelligent Fluid Mechanics, Harbin Institute of Technology, Harbin 150001, China*
[3]*National Key Laboratory of Ship Structural Safety, Harbin 150001, China*
[4]*College of Shipbuilding Engineering, Harbin Engineering University, Harbin 150001, China*
[5]*State Key Laboratory of Engine, Tianjin University, Tianjin 300350, China*
[6]*Molinaroli College of Engineering and Computing, University of South Carolina, South Carolina 29063, USA*
[7]*School of Mechanical and Electrical Engineering, Gui Lin University of Electronic Technology, Gui Lin 541004, China*
[8]*School of Civil Engineering, Shandong University, Jinan 250061, China*
[9]*School of Civil Engineering, Harbin Institute of Technology, Harbin 150001, China*

(Received 18 September 2025; accepted 24 July 2026; published 24 August 2026)

Wall slip is ubiquitous in molten polymer flows, yet its role in polymer diffusive instability (PDI)—a unique viscoelastic instability driven by polymer stress diffusion at vanishing Reynolds numbers—remains uncharacterized. Here, we combine linear stability analysis and direct numerical simulations (DNS) to investigate PDI in viscoelastic plane Poiseuille flow under Navier slip conditions ($u = b\tau_{xy}$). Four distinct PDI modes are identified: PDI-1 (negative phase velocity, including antisymmetric PDI-1a and symmetric PDI-1s) and PDI-2 (positive phase velocity, including PDI-2a and PDI-2s). Wall slip exerts differential regulatory effects: it stabilizes PDI-1 (PDI-1s fully stabilizes at $b = 0.003$) but triggers PDI-2 instability under small b. Energy balance analysis reveals PDI-1 is dominated by base-state conformation tensor contributions, while PDI-2 is driven by base-state velocity gradients. DNS validates these linear predictions, showing consistent nonlinear evolution for symmetric/antisymmetric perturbations. Our findings provide a quantitative basis for PDI control in polymer processing.

DOI: 10.1103/l1vn-44b3

I. INTRODUCTION

Viscoelastic fluids frequently exhibit flow instability in scenarios where Newtonian fluids remain stable, a phenomenon driven by the nonlinear coupling between elastic and viscous stresses [1,2]. Polymer stress diffusion is frequently incorporated in viscoelastic simulations to regularize hyperbolic constitutive relationships [3–8], and this approach has also led to the discovery of a distinct instability mechanism: polymer diffusive instability (PDI). PDI can occur at vanishing Reynolds number and requires shear, finite polymer stress diffusion, and a wall boundary to occur. This unique instability, distinct from inertia-driven or purely elastic instabilities, has attracted considerable attention since its first demonstration by Beneitez *et al.* [9] using Oldroyd-B and

*Contact author: shaoweiwang@sdu.edu.cn
†Contact author: z.ding@hit.edu.cn

FENE-P models under no-slip boundary conditions. Their work revealed that even a small nonzero polymer stress diffusivity can trigger a linear instability, evolving into a self-sustaining 3D chaotic state in inertialess shear flows—marking a unique observation of such behavior in wall-bounded parallel viscoelastic flows.

Subsequent investigations have deepened insights into PDI's intrinsic characteristics and the range of factors shaping its occurrence and evolution. Couchman *et al.* [10] explored inertial effects on PDI in plane Couette and Poiseuille flows, showing that increasing inertia broadens the instability's parameter space and enhances growth rates, lowering the critical Weissenberg number ($\mathrm{Wi_c}$) and diffusivities required for onset. Lewy and Kerswell [11] linked PDI to short-wavelength surface phenomena—such as the "sharkskin" instability in highly concentrated polymeric fluids—noting that both are short-wavelength instabilities localized to the extrudate surface. They further demonstrated that inertia exerts a destabilizing effect: it reduces the minimum Wi required for PDI to occur, lowering it from eight (observed in inertialess flows) to two when inertial effects become significant. Additionally, Beneitez *et al.* [12] identified a common Ruelle-Takens transition pathway for elastic turbulence (ET) and elastoinertial turbulence (EIT) in FENE-P fluids, where PDI initiates bifurcations leading to chaos, with secondary large-scale instabilities (resembling "center" and "wall" modes) modulating the chaotic dynamics. This interpretation differs fundamentally from that of Khalid *et al.* [13]: they regard the central mode [14,15] as the core continuous pathway connecting ET and EIT, independent of PDI. Pandey and Shankar [16] found that anisotropic mobility influences diffusion instability in viscoelastic shear flows, noting that mobility anisotropy can alter the energy exchange between base flow and perturbations.

A critical factor in polymer flow dynamics that remains underexplored in the context of PDI is wall slip—the phenomenon where fluid velocity at the wall differs from the wall's velocity (in contrast to the traditional no-slip assumption). The flow stability induced by wall slip has been extensively studied across diverse fluid types and flow models [17–20]. Molten polymers often exhibit significant slip when wall shear stress exceeds a critical threshold [21], influencing both flow stability [22–24] and rheological property measurements [25]. Wall slip is commonly modeled using Navier's law, which relates slip velocity to wall shear stress [24]: $\mathbf{u}_w = b^* \tau_w$, where b^* is a slip coefficient dependent on temperature, normal stress, and fluid-wall interactions. Previous studies have shown that slip can induce or modify viscoelastic instabilities [26–28], with Pal and Samanta [29] noting that slip length stabilizes shear modes in Walters' liquid B'' flow, while viscoelastic parameters promote destabilization.

Despite these insights, the interplay between wall slip and PDI remains uncharacterized. Wall slip directly alters the shear stress distribution near the wall (via Navier's law), which in turn modifies the base-state polymer conformation tensor and its gradient—two core factors governing PDI's energy exchange process. Given slip's prevalence in polymer flows and PDI's unique role in triggering chaos at low Reynolds numbers, understanding how slip parameters modulate PDI is essential for refining instability predictions in practical processing scenarios. The remainder of this investigation is outlined as follows. Section II details the mathematical formulation and linear stability governing equations, Sec. III presents theoretical findings on critical properties, Sec. IV describes direct numerical simulations, and Sec. V summarizes key results and outlines future work.

II. MATHEMATICAL FORMULATION

We consider the inertialess, pressure-driven flow between two infinitely long and wide parallel plates separated by a distance $2H$. A schematic of the geometry and reference frame is shown in Fig. 1. The dimensionless governing equations for this system are given by

$$\nabla p = \beta \Delta \mathbf{u} + (1-\beta)\nabla \cdot \mathbf{T}(\mathbf{C}), \tag{1}$$

$$\nabla \cdot \mathbf{u} = 0, \tag{2}$$

$$\partial_t \mathbf{C} + (\mathbf{u}\cdot\nabla)\mathbf{C} + \mathbf{T}(\mathbf{C}) = \mathbf{C}\cdot\nabla\mathbf{u} + (\nabla\mathbf{u})^T \cdot \mathbf{C} + \varepsilon \nabla^2 C, \tag{3}$$

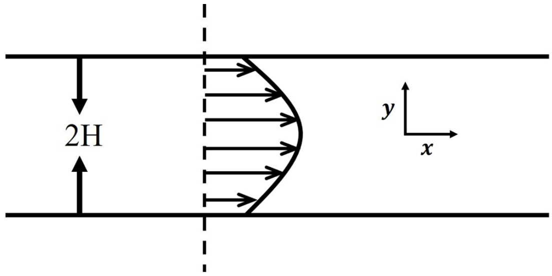

FIG. 1. Schematic representation of pressure-driven flow in a channel.

where the polymeric stress tensor $\mathbf{T}$ is related to the conformation tensor $\mathbf{C}$ via the Oldroyd-B model as

$$\mathbf{T} = \frac{1}{\mathrm{Wi}}(\mathbf{C} - \mathbf{I}). \tag{4}$$

For the FENE-P model, the corresponding relation reads

$$\mathbf{T}(\mathbf{C}) := \frac{1}{\mathrm{Wi}}\left[\frac{\mathbf{C}}{1 - (\mathrm{tr}\,\mathbf{C} - 3)/L_{\mathrm{max}}^2} - \mathbf{I}\right]. \tag{5}$$

In the present study, we mainly focus on the Oldroyd-B model. These equations are rendered dimensionless using the channel's half-width H as the unit of length, the centerline maximum velocity U_0 of the laminar profile as the unit velocity, and H/U_0 as the unit time. The dimensionless parameters in the governing equations are the Weissenberg number $\mathrm{Wi} = \frac{\lambda U_0}{H}$, the dimensionless polymer diffusivity $\varepsilon = \frac{D}{U_0 H}$ (where D is the polymer diffusivity), and the ratio of solvent viscosity to the total viscosity $\beta = \frac{\eta_s}{\eta}$.

In this study, dimensionless velocity slip conditions and stress nondiffusion conditions are applied to the boundaries:

$$\begin{gathered} y = \pm 1 : u = \mp b(\beta \partial_y u + (1-\beta) T_{xy}), \\ v = 0, \quad \nabla^2 \mathbf{T} = 0, \end{gathered} \tag{6}$$

where b is the dimensionless slip coefficient. The $\nabla^2 \mathbf{T} = 0$ condition follows the classic assumption for polymer stress diffusion in wall-bounded flows, which enforces "no flux of stress diffusion" at the wall [11] (i.e., the second derivative of stress—related to diffusion flux gradient—vanishes). The laminar base state of interest is the steady, fully developed pressure-driven channel flow. With the centerline velocity as the velocity scale, the pressure gradient is adjusted so that $U|_{y=0} = 1$. The base state is described by

$$U = 1 - \frac{1}{2b+1} y^2, \quad V = 0, \quad C_{xy} = -\frac{\mathrm{Wi}}{2b+1} y, \quad C_{yy} = 1, \tag{7}$$

$$C_{xx} = \frac{8\mathrm{Wi}^2 y^2}{(2b+1)^2} + \frac{16\varepsilon \mathrm{Wi}^3}{(2b+1)^2}\left(1 - \frac{\cosh(y/\sqrt{\varepsilon \mathrm{Wi}})}{\cosh(1/\sqrt{\varepsilon \mathrm{Wi}})}\right). \tag{8}$$

If the dimensionless slip length is defined as $l = l^*/H$ (where l^* denotes the dimensional slip length), b can be simply related to this dimensionless slip length l via the relation $b = (l^2 + 2l)/2$. This relation is derived based on the characteristics of the steady, fully developed pressure-driven channel flow described by the above base state [Eq. (7)].

A temporal linear stability analysis of the base flow is conducted by introducing infinitesimal perturbations. Thus, the flow variables are expressed as $\mathbf{u} = \mathbf{u_0} + \mathbf{u}'$, $\mathbf{C} = \mathbf{C_0} + \mathbf{C}'$, and $p = p'$, where $\mathbf{u_0}$ and $\mathbf{C_0}$ are the base state. The perturbations are organized as $\mathbf{q}' = [u', v', p', c'_{xx}, c'_{xy}, c'_{yy}]$, and are decomposed into

$$\mathbf{q}' = \hat{\mathbf{q}}(y)\exp^{i(\alpha x-\omega t)}, \tag{9}$$

where α is the dimensionless wave number and ω is the complex frequency. The perturbation equations governing the stability of the base state lead to a generalized eigenvalue problem

$$\mathrm{i}\alpha\hat{u} + D\hat{v} = 0, \tag{10}$$

$$\alpha\hat{p} = \beta(D^2-\alpha^2)\hat{u} + \frac{1-\beta}{\mathrm{Wi}}(\mathrm{i}\alpha\hat{c}_{xx} + D\hat{c}_{xy}), \tag{11}$$

$$D\hat{p} = \beta(D^2-\alpha^2)\hat{v} + \frac{1-\beta}{\mathrm{Wi}}(\mathrm{i}\alpha\hat{c}_{xy} + D\hat{c}_{yy}), \tag{12}$$

$$\frac{\hat{c}_{xx}}{\mathrm{Wi}} - \mathrm{i}\omega\hat{c}_{xx} + \mathrm{i}\alpha U\hat{c}_{xx} + DC_{xx}\hat{v} = \varepsilon(D^2-\alpha^2)\hat{c}_{xx} + 2\mathrm{i}\alpha C_{xx}\hat{u} + 2C_{xy}D\hat{u} + 2DU\hat{c}_{xy}, \tag{13}$$

$$\frac{\hat{c}_{xy}}{\mathrm{Wi}} - \mathrm{i}\omega\hat{c}_{xy} + \mathrm{i}\alpha U\hat{c}_{xy} + DC_{xy}\hat{v} = \varepsilon(D^2-\alpha^2)\hat{c}_{xy} + DU\hat{c}_{yy} + \mathrm{i}\alpha C_{xx}\hat{v} + D\hat{u}, \tag{14}$$

$$\frac{\hat{c}_{yy}}{\mathrm{Wi}} - \mathrm{i}\omega\hat{c}_{yy} + \mathrm{i}\alpha U\hat{c}_{yy} = \varepsilon(D^2-\alpha^2)\hat{c}_{yy} + 2\mathrm{i}\alpha C_{xy}\hat{v} + 2D\hat{v}. \tag{15}$$

Here, $D = \frac{d}{dy}$. We discretize the perturbation equations [together with the boundary conditions in (6)] using a Chebyshev spectral collocation method: eigenfunctions are expanded in Chebyshev series, which are then substituted into the governing equations and evaluated at Gauss-Lobatto points. The resulting generalized eigenvalue problem is solved using the QZ method, ensuring sufficient spatial resolution for eigenvalue convergence. All parametric studies in this work are conducted with a fixed solvent-to-total viscosity ratio of $\beta = 0.8$.

III. LINEAR STABILITY ANALYSIS

In Fig. 2, we present examples of such instabilities by plotting the eigenvalue spectra for $\mathrm{Wi} = 120$, $\alpha = 1.6$, and $\varepsilon = 0.001$ under no-slip conditions. The shape of the eigenvalue spectrum is consistent with that reported by Couchman *et al.* [10]. However, under these parameters, we identify four unstable eigenvalues that were not reported previously. To distinguish these four eigenvalues, we classify them according to two key characteristics. Modes with negative phase velocity ($c_r = \omega_r/\alpha < 0$, propagating in the $-x$ direction) are labeled PDI-1, whereas those with positive phase velocity ($c_r > 0$, propagating in the $+x$ direction) are labeled PDI-2. Based on the symmetry of the streamwise velocity perturbation $u'(y)$ [Fig. 2(b)], antisymmetric modes satisfy $u'(y) = -u'(-y)$ (suffix "a"), while symmetric modes satisfy $u'(y) = u'(-y)$ (suffix "s"). Table I compares the converged eigenvalues obtained using different collocation resolutions for both Oldroyd-B and FENE-P fluids. The FENE-P results are computed with $L_{\max} = 500$, while the remaining parameters are identical to those used in Fig. 2. The distinct converged eigenvalues of the symmetric and antisymmetric branches confirm that these modes are physically distinct and not numerical artifacts.

Previous studies of PDI in wall-bounded shear flows have mainly emphasized the branch that we denote here as PDI-1 [9–11]. In the no-slip Poiseuille problem, the PDI-2 branch is much harder to detect because its critical Weissenberg number is substantially larger than that of PDI-1. The present work shows that wall slip changes this hierarchy: PDI-1 is progressively stabilized by slip, whereas PDI-2 can become the dominant unstable branch over a finite range of slip. This slip-induced exchange of dominant PDI branch has not been reported much previously. The differences between the symmetric and antisymmetric branches are primarily confined to the channel centerline, while their near-wall structures remain nearly identical [see Fig. 2(b)]. Since PDI is fundamentally a near-wall instability associated with a localized elastic boundary layer [9], the symmetry of the eigenfunctions has only a weak influence on the instability characteristics. This conclusion is further supported by

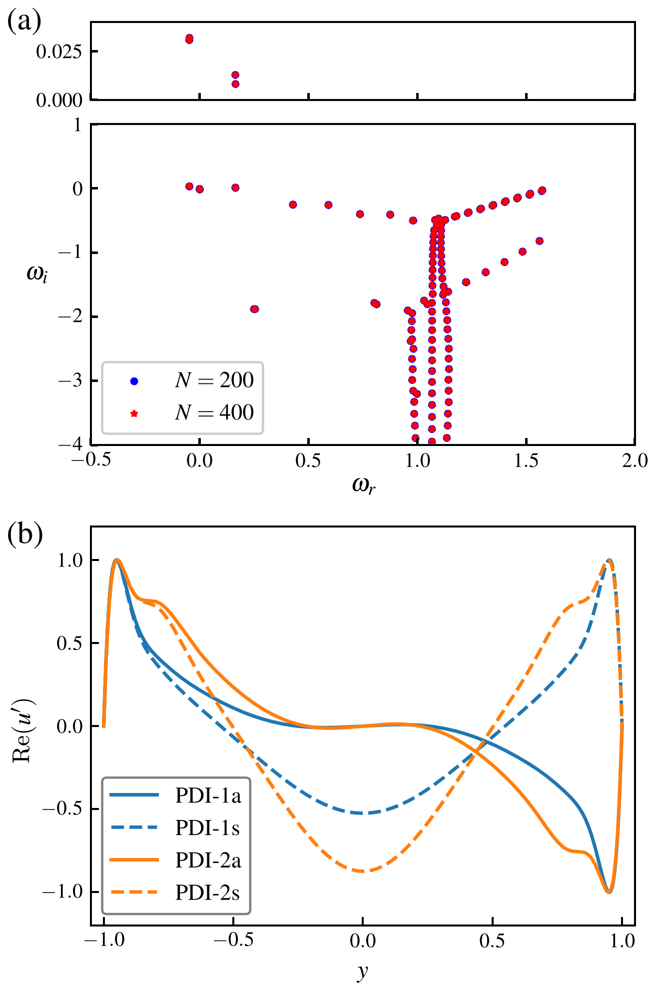

FIG. 2. (a) Spectrum at Wi $= 120$, $\alpha = 1.6$, and $\varepsilon = 0.001$ for two different resolutions $N = 200$ (blue dots) and $N = 400$ (red dots). Top inset: Zoom-in to the unstable eigenvalues $\omega_i > 0$ (b) The eigenfunctions.

TABLE I. Comparison of the converged eigenvalues of symmetric and antisymmetric modes under different numbers of collocation points for Oldroyd-B and FENE-P fluids. Unless otherwise specified, the parameters are Wi $= 120$, $\alpha = 1.6$, and $\varepsilon = 0.001$. The FENE-P results are obtained with $L_{\max} = 500$.

Fluid	Mode	$N = 200$	$N = 400$	$N = 600$
Oldroyd-B	PDI-1a	$-0.046641 + 0.031906\,i$	$-0.046641 + 0.031906\,i$	$-0.046640 + 0.031906\,i$
	PDI-1s	$-0.047361 + 0.030766\,i$	$-0.047361 + 0.030766\,i$	$-0.047360 + 0.030766\,i$
	PDI-2a	$0.164209 + 0.012851\,i$	$0.164209 + 0.012851\,i$	$0.164209 + 0.012851\,i$
	PDI-2s	$0.164930 + 0.008153\,i$	$0.164930 + 0.008153\,i$	$0.164930 + 0.008153\,i$
FENE-P	PDI-1a	$-0.052551 + 0.015864\,i$	$-0.052551 + 0.015864\,i$	$-0.052551 + 0.015864\,i$
	PDI-1s	$-0.052682 + 0.014960\,i$	$-0.052682 + 0.014960\,i$	$-0.052682 + 0.014961\,i$
	PDI-2a	$0.185330 - 0.022753\,i$	$0.185330 - 0.022753\,i$	$0.185330 - 0.022753\,i$
	PDI-2s	$0.185861 - 0.026728\,i$	$0.185861 - 0.026727\,i$	$0.185861 - 0.026728\,i$

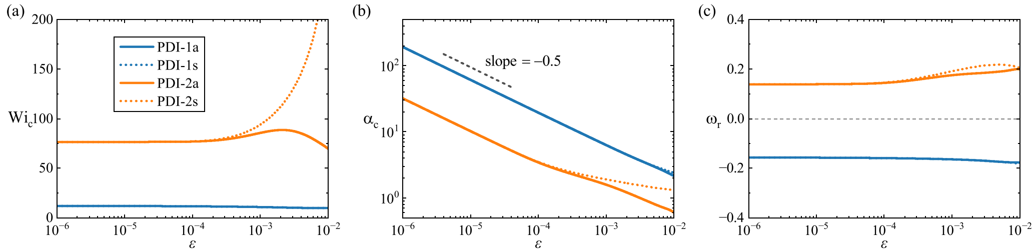

FIG. 3. The critical parameters for different ε for all four modes under no-slip conditions are presented. Solid and dashed lines denote the "a" and "s" modes, respectively. (a) shows the critical $\mathrm{Wi_c}$, (b) presents the critical wave number α_c, and (c) depicts the frequency ω_r.

both the linear stability analysis and the DNS results, which show nearly identical growth behavior and nonlinear saturated states for the symmetric and antisymmetric branches of the same PDI family. Moreover, these modes occur at vanishing Reynolds number, require finite polymer diffusion, and are wall localized. They are therefore different from inertial Tollmien-Schlichting-type modes, from purely elastic instabilities that do not rely on polymer diffusion, and from the center-mode scenario discussed in the ET/EIT literature.

The neutral curves are presented in Fig. 3 for various ε. For small ε, the neutral curves track a constant $\mathrm{Wi_c}$ for both PDI-1 and PDI-2, and the "a" and "s" modes converge to the same $\mathrm{Wi_c}$ value. The corresponding critical wave number gradually increases with $\varepsilon \to 0$, approximately following the scaling relation $\alpha_c \propto \varepsilon^{-1/2}$. When ε is large, the PDI-2a mode exhibits a lower critical $\mathrm{Wi_c}$ than the PDI-2s mode. As shown in Fig. 3(c), PDI-1 and PDI-2 have frequencies of approximately the same magnitude but opposite signs, and they do not vary significantly with ε.

The slip coefficient b may have different effects on these four modes. Neutral curves for PDI-1 and PDI-2 with different ε are shown in Fig. 4. Both the PDI-1a and PDI-1s modes become more

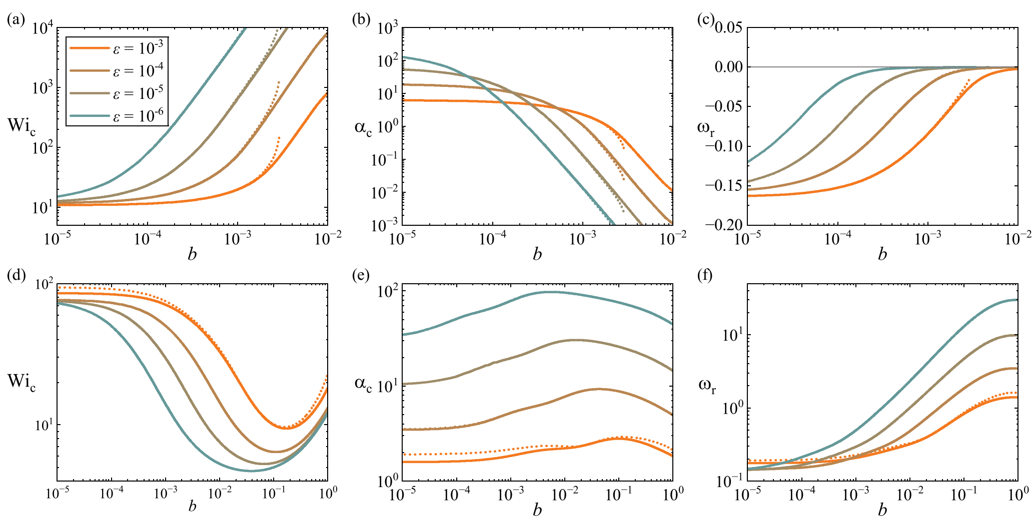

FIG. 4. Critical instability parameters as functions of the slip coefficient b for different polymer diffusivities ε. Colors denote different values of ε, while solid and dashed lines represent antisymmetric and symmetric modes, respectively. Panels (a)–(c) correspond to the PDI-1 branch, showing the critical Weissenberg number $\mathrm{Wi_c}$, the critical wave number α_c, and the real frequency ω_r, respectively. Panels (d)–(f) show the corresponding quantities for the PDI-2 branch.

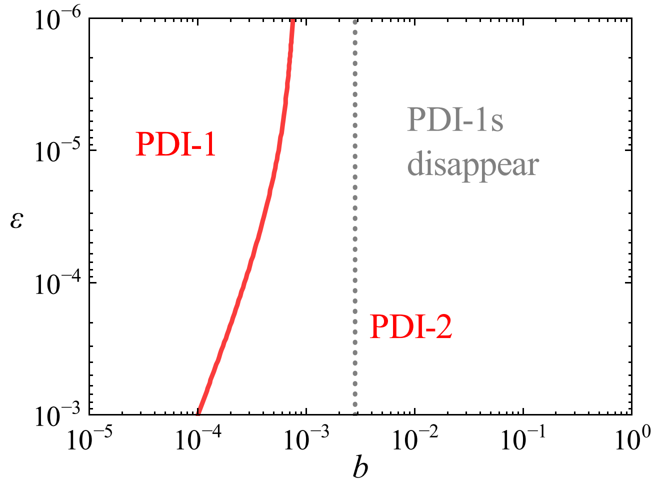

FIG. 5. Dominant PDI mode evolution with b. The red curve denotes the boundary between parameter ranges of dominant PDI modes, while the dashed line indicates the threshold beyond which PDI-1a is stabilized with increasing b.

stable as b increases. In this process, the frequency approaches 0 from a negative value, and the wave number decreases. The critical $\mathrm{Wi_c}$ for the PDI-1a mode is higher than that for the PDI-1s mode, and the difference between the two increases with increasing b. When b reaches 0.003, the PDI-1s mode stabilizes and disappears from the plane. A higher ε corresponds to a lower critical $\mathrm{Wi_c}$ and frequency.

For PDI-2 mode, the critical $\mathrm{Wi_c}$ for different ε decreases first and then increases with increasing b, and the minimum value corresponding to b increases with increasing ε. Similar to PDI-1, the critical parameters of PDI-2a and PDI-2s modes are basically the same, but the critical $\mathrm{Wi_c}$ of PDI-2s is slightly higher than that of PDI-2a mode. Furthermore, as ε increases, the critical wave number significantly decreases.

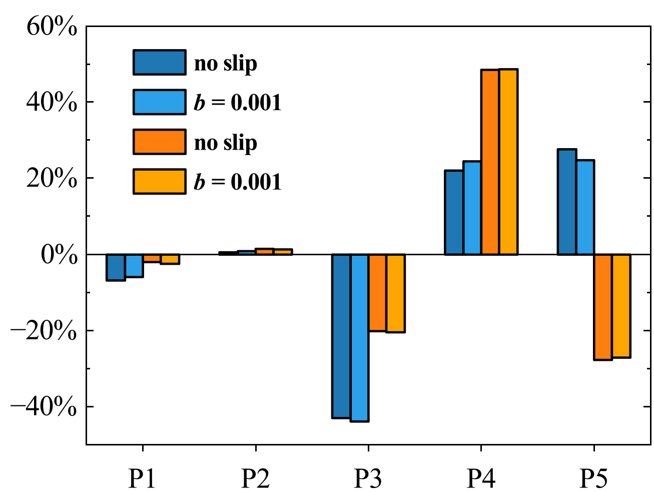

FIG. 6. Perturbation amplitude balance terms for PDI-1a (blue) and PDI-2a (orange) modes, showing their relative contributions.

To further clarify the slip-dependent selection of PDI modes, Fig. 5 summarizes the evolution of dominant instability branches across the parameter space of b and ε. The red curve delineates the boundary between the regions dominated by the PDI-1 family and the PDI-2 family, respectively, while the dashed vertical line represents the independent threshold for the stabilization and disappearance of PDI-1s. Specifically, for small b, the PDI-1 family prevails as the dominant unstable mode within the region bounded by the red curve. As b increases past the dashed vertical threshold, PDI-1s is fully stabilized and disappears from the unstable mode set; as b crosses the boundary marked by the red curve, the PDI-2 family emerges as the dominant unstable mode.

The destabilization of flow disturbances is usually affected by the various energy transfer mechanisms. To extract possible underlying physical mechanisms behind the stability characteristics of PDI, we analyze the perturbation energy balance. Doering *et al.* [30] demonstrated that conventional energy stability analysis cannot be directly extended to Oldroyd-B fluids. Instead, we employ the L^2 norm of the polymer configuration tensor $\hat{\mathbf{c}}$ as an effective measure of perturbation amplitude in purely elastic flows:

$$
\begin{aligned}
&\omega_i \int (\hat{c}_{xx}\hat{c}_{xx}^* + \hat{c}_{xy}\hat{c}_{xy}^* + \hat{c}_{yy}\hat{c}_{yy}^*)\mathrm{d}y \\
&\quad = \underbrace{-\frac{1}{\mathrm{Wi}} \int (\hat{c}_{xx}\hat{c}_{xx}^* + \hat{c}_{xy}\hat{c}_{xy}^* + \hat{c}_{yy}\hat{c}_{yy}^*)dy}_{P1} \underbrace{- \int \mathrm{Re}(DC_{xx}\hat{v}\hat{c}_{xx}^* + DC_{xy}\hat{v}\hat{c}_{xy}^*)dy}_{P2} \\
&\quad \underbrace{-\alpha \int \mathrm{Im}\big(2C_{xx}\hat{u}\hat{c}_{xx}^* + C_{xx}\hat{v}\hat{c}_{xy}^* + 2C_{xy}\hat{v}\hat{c}_{yy}^*\big)dy + \int \mathrm{Re}\big(2C_{xy}D\hat{u}\hat{c}_{xx}^* + D\hat{u}\hat{c}_{xy}^* + 2D\hat{v}\hat{c}_{yy}^*\big)dy}_{P3} \\
&\quad + \underbrace{\int \mathrm{Re}\big(2DU\,\hat{c}_{xy}\hat{c}_{xx}^* + DU\,\hat{c}_{yy}\hat{c}_{xy}^*\big)dy}_{P4} \\
&\quad + \underbrace{\varepsilon \int \big[\big(D^2\hat{c}_{xx}\hat{c}_{xx}^* + D^2\hat{c}_{xy}\hat{c}_{xy}^* + D^2\hat{c}_{yy}\hat{c}_{yy}^*\big) - \alpha^2\big(\hat{c}_{xx}\hat{c}_{xx}^* + \hat{c}_{xy}\hat{c}_{xy}^* + \hat{c}_{yy}\hat{c}_{yy}^*\big)\big]dy}_{P5}.
\end{aligned}
$$

Here, P2 denotes the contribution from the gradient of the base-state conformation tensor, P3 denotes the contribution from the base-state conformation tensor itself, P4 denotes the contribution from the base-state velocity gradient, and P5 denotes the contribution from polymer diffusivity.

As shown in Fig. 6, the perturbation amplitude balance terms for PDI-1a and PDI-2a are compared (the "a" and "s" modes exhibit nearly identical energy-budget characteristics and therefore only the antisymmetric modes are shown). The instability dynamics are primarily governed by the balance among P3, P4, and P5, whereas the contributions from P1 and P2 remain negligible.

For the PDI-1 branch, the instability behaves as a diffusion-regularized elastic boundary-layer mode sustained by the release of elastic energy stored within the near-wall polymer-stress layer. In the Oldroyd-B base state, the streamwise polymer stretch C_{xx} develops a highly localized near-wall layer whose thickness is controlled by polymer diffusion and Wi. The PDI-1 eigenfunctions are strongly concentrated within this region and extract energy predominantly from the spatially inhomogeneous polymer configuration field. Physically, perturbations redistribute highly stretched polymers inside the near-wall elastic layer, while stress diffusion couples this redistribution to the perturbation stress field. This interpretation is consistent with the dominant contribution of the P3 term, which represents direct energy transfer from the base polymer conformation field to the perturbations.

Wall slip strongly modifies this mechanism through its influence on the near-wall shear. Since the base shear scales as $\partial_y U \sim (2b+1)^{-1}$, increasing slip simultaneously reduces both the magnitude and the wall-normal gradients of the base polymer stresses. Consequently, the elastic energy stored

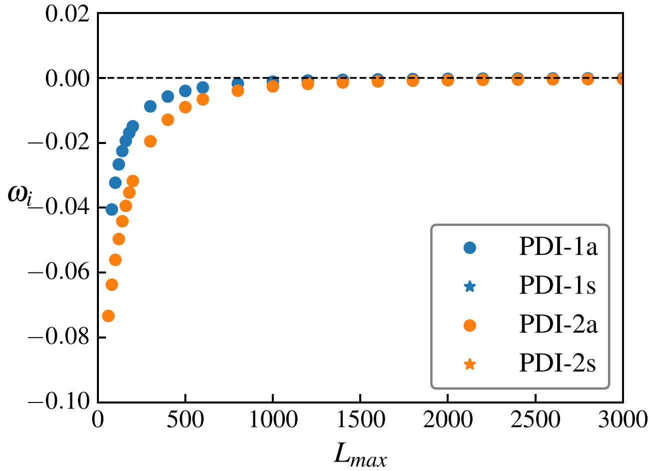

FIG. 7. Growth rate ω_i vs $L_{\max}$ for FENE-P fluids at $\varepsilon = 10^{-4}$ and $b = 10^{-3}$, with α and Wi taken from Oldroyd-B fluids' critical stability values at these parameters.

inside the near-wall layer decreases substantially as the slip coefficient increases, thereby weakening the energy source sustaining PDI-1. In addition, the critical wave number decreases with increasing slip, indicating weaker wall localization of the perturbation field, which further suppresses the instability.

By contrast, the PDI-2 branch is governed mainly by coupling between perturbation stresses and the mean velocity gradient, corresponding to the dominant P4 contribution. The instability is sustained through shear-induced tilting and reorientation of perturbation stresses by the base shear and therefore behaves more like a shear-driven elastic mode than a stress-layer instability. Because this mechanism depends more directly on kinematic coupling with the mean shear and less on localized stress accumulation, it is less sensitive to the reduction of near-wall stress gradients induced by slip. Moreover, moderate slip weakens the confinement imposed by the no-slip wall and reduces wall-induced diffusive damping, allowing the PDI-2 branch to become unstable at lower critical Wi_c. At sufficiently large slip, however, the shear-driven elastic mechanism itself becomes too weak and the instability is restabilized.

The opposite energy contribution of the polymer-diffusion term to the two branches reflects the different phase relations between the diffusive stress flux and the perturbation field. For PDI-1, diffusion redistributes polymer stress across the thin elastic boundary layer in a manner that reinforces the perturbation structure, giving a positive contribution to the energy budget. For PDI-2, however, diffusion acts mainly to smooth the stress perturbations associated with shear-induced reorientation, thereby extracting perturbation energy and producing a negative contribution.

Finally, we briefly examine the influence of finite polymer extensibility on PDI under slip conditions using the FENE-P model. Figure 7 shows the growth rate ω_i as a function of the maximum polymer extensibility $L_{\max}$ for $\varepsilon = 10^{-4}$ and $b = 10^{-3}$, with α and Wi fixed at the corresponding critical values obtained from the Oldroyd-B model. As $L_{\max}$ increases, the growth rates approach the Oldroyd-B results, indicating that finite-extensibility effects become negligible in the large-$L_{\max}$ limit. In contrast, smaller $L_{\max}$ significantly suppresses the instability, with a stronger stabilizing effect observed for PDI-2 than for PDI-1. Finite extensibility limits large polymer stretch and therefore weakens the elastic feedback sustaining the instability. Since PDI-1 is governed mainly by energy extraction from the near-wall polymer-stress layer, its destabilization mechanism remains partially preserved even under bounded stretch. By contrast, PDI-2 relies more directly on shear-induced reorientation and amplification of perturbation stresses, making its shear-driven amplification mechanism more sensitive to the reduction of polymer extensibility. These results

TABLE II. Comparison of $\langle E_k' \rangle$ at different time instants for PDI-1a and PDI-2a modes under different grid resolutions.

	(N_x, N_y)	$t = 500$	$t = 1000$	$t = 1500$
PDI-1a	(384, 384)	8.919×10^{-6}	2.778×10^{-3}	2.304×10^{-2}
PDI-1a	(512, 600)	8.919×10^{-6}	2.778×10^{-3}	2.304×10^{-2}
PDI-1a	(768, 768)	8.919×10^{-6}	2.781×10^{-3}	2.304×10^{-2}
PDI-2a	(384, 384)	6.724×10^{-4}	3.123×10^{-1}	3.123×10^{-1}
PDI-2a	(512, 600)	6.721×10^{-4}	3.123×10^{-1}	3.123×10^{-1}
PDI-2a	(768, 768)	6.723×10^{-4}	3.123×10^{-1}	3.123×10^{-1}

suggest that polymer chain extensibility can substantially influence both the onset and the dominant mechanism of PDI in realistic polymer flows.

IV. DIRECT NUMERICAL SIMULATION

Then, we present a direct numerical simulation (DNS) study of the PDI modes. The nonlinear evolution of PDI is analyzed by performing 2D DNS of the governing Eq. (3), which incorporate polymer stress diffusion, using the open-source code DEDALUS [31]. The quantities $\mathbf{C}$ and $\mathbf{u}$ are expanded using Fourier modes in the x direction and Chebyshev modes in the y direction. We consider a computational domain of fixed size $[L_x, L_y] = [2\pi, 2]$, and use $N_x = 512$ and $N_y = 600$ for the numbers of Fourier and Chebyshev modes, respectively. Time integration is carried out using a third-order semi-implicit BDF scheme [32] with a fixed time step.

The average kinetic energy of the perturbation velocity field ($\langle E_k' \rangle$) is defined as $\langle E_k' \rangle = \frac{1}{2}\langle \mathbf{u}' \cdot \mathbf{u}' \rangle$, where $\langle \cdot \rangle$ denotes the volume average. The initial conditions of the simulation consist of the base flow superimposed with perturbations derived from linear stability analysis. Based on the results of the modal analysis, the amplitude of the initial perturbation is carefully calibrated to ensure $\langle E_k' \rangle < 10^{-7}$, thereby guaranteeing a sufficiently prolonged linear growth phase during DNS evolution. In Table II, we compare $\langle E_k' \rangle$ at various instants for the two cases investigated under different grid resolutions, which verifies that the grid resolution adopted in the present study is sufficient.

It is worth noting that, although the initial perturbation fields corresponding to PDI-1a and PDI-1s have opposite symmetries, their temporal evolution patterns are quite similar. First, we computed the results of PDI-1 under parameters $\alpha_c = 2$, $\varepsilon = 10^{-3}$, $b = 10^{-3}$, and $\mathrm{Wi} = 30$, which the modal analysis suggests very close growth rates of 0.00506 and 0.00477 for PDI-1a and PDI-1s, respectively. The average kinetic energy of the perturbation velocity field ($\langle E_k' \rangle$) and the volume-averaged polymer stretch field are shown in Fig. 8(a).

Initially, within the time range $0 \leqslant t \leqslant 750$, the $\langle E_k' \rangle$ grows exponentially, while $\langle \mathrm{tr}(\mathbf{C}) \rangle$ remains relatively constant. Subsequently, the growth rate of $\langle E_k' \rangle$ starts to exceed exponential growth. However, as time went by, this growth rate gradually slowed down, and eventually $\langle E_k' \rangle$ stabilized at a constant value. During the period when t varies from 1000 to 1500, the value of $\langle \mathrm{tr}(\mathbf{C}) \rangle$ witnesses a rapid growth. Moreover, both the growth rate and the final stable value of PDI-1a are slightly larger than those of PDI-1s. Meanwhile, in Fig. 8(b), we present x-direction averaged values of the flow field. It is found through analysis that the average values of the flow field data of PDI-1a and PDI-1s are also basically the same.

We also considered a case of the PDI-2 mode with the slip condition. Parameters are set to $\alpha_c = 8$, $\varepsilon = 10^{-4}$, $b = 10^{-2}$, and $\mathrm{Wi} = 18$, for which the modal analysis suggests a growth rate of 0.0084 for both PDI-2a and PDI-2s. The relevant results are plotted in Fig. 9.The results of PDI-2 are basically the same as those of PDI-1. The difference is that the linear growth stage of PDI-2 is shorter, only occurring in the initial period when $t < 200$. In addition, when $t = 2000$, the flow field undergoes a short period of irregular oscillations. The averaged quantities are more localized near the wall than those of PDI-1.

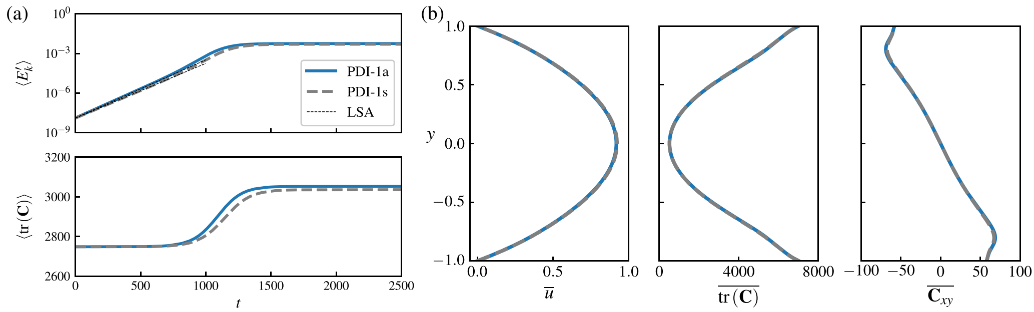

FIG. 8. Direct numerical simulations for Wi $= 30$, $\alpha_c = 2$, $\varepsilon = 10^{-3}$, and $b = 10^{-3}$ for PDI-1a and PDI-1s modes. (a) The growth rate of the perturbation velocity field and the volume-averaged polymer stretch field. (b) Averaged quantities in the x direction at nonlinear saturation.

Figures 10(c) and 10(d) present the nonlinear saturated contours of PDI-2. Unlike those of PDI-1 [Figs. 10(a) and 10(b)], the nonlinear saturated periodic oscillatory states of PDI-2 are irrelevant to the wave number and frequency derived from linear stability analysis. Two localized structures can be observed, concentrated near the upper and lower walls of the flow field. Additionally, in the contour plot of tr$(\mathbf{C})$ for PDI-2, a distinct "long tail" feature is present in the downstream region.

In a recent study by Beneitez *et al.* [12], it was pointed out that finite-amplitude, small-scale traveling waves localized near the wall and generated by PDI correspond to a secondary instability that drives large-scale flow dynamics. This secondary instability can trigger elastic turbulent (ET) or elastic-inertial turbulent (EIT) regimes, with its unstable wave structures resembling the "center" and "wall" mode instabilities. It is also shown by them that the wavelength corresponding to the secondary instability is much longer than that of the primary instability. In our study, the flow evolves into a localized structure, which is, however, steady, suggesting that PDI remains stable in the present numerical simulation. However, we suspect that the PDI may be unstable to perturbations with much longer wavelength, similar to Beneitez *et al.* [12], or spanwise perturbations, which may also trigger ET. However, resolving the secondary instability is numerically challenging and computationally expensive, since either a 2D global stability analysis is required or a 3D biglobal stability analysis is required.

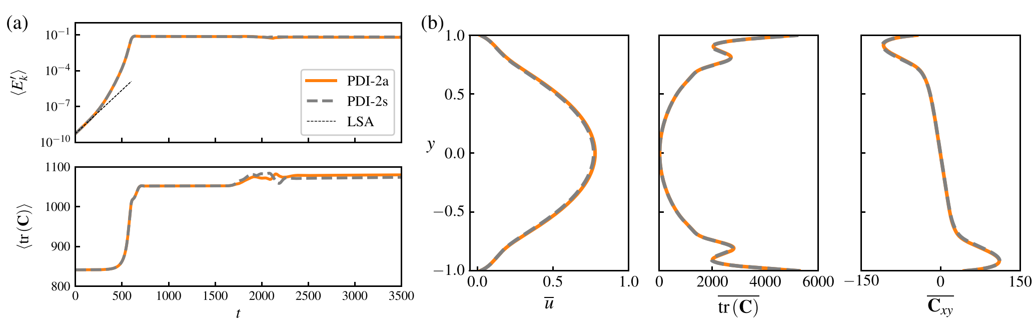

FIG. 9. Direct numerical simulations for Wi $= 18$, $\alpha_c = 8$, $b = 10^{-2}$, and $\varepsilon = 10^{-4}$ for PDI-2a and PDI-2s modes. (a) The growth rate of the perturbation velocity field and the volume-averaged polymer stretch field. (b) Averaged quantities in the x direction at nonlinear saturation.

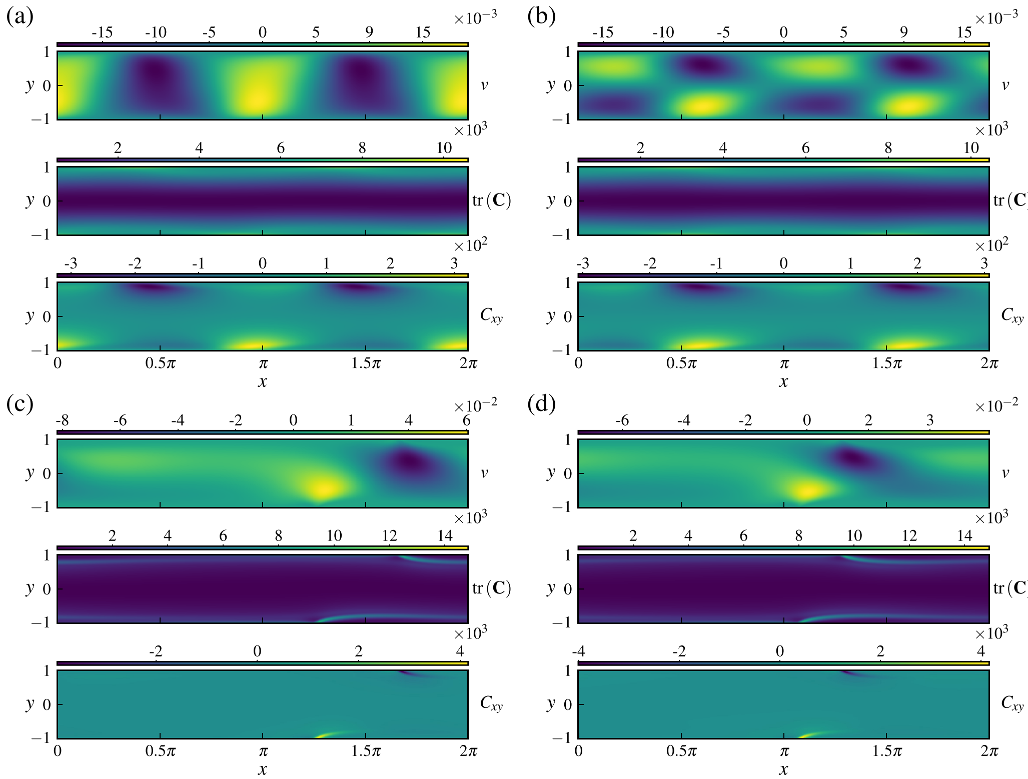

FIG. 10. The contour of u', v', and tr($\mathbf{C}$) at nonlinear saturation: (a) PDI-1a, (b) PDI-1s, (c) PDI-2a, and (d) PDI-2s.

V. DISCUSSION AND CONCLUSIONS

This study investigates PDI in viscoelastic Poiseuille flow under slip boundary conditions, revealing key insights through linear stability analysis and direct numerical simulations.

We identify four distinct PDI modes, categorized by phase velocity (PDI-1 with negative phase velocity and PDI-2 with positive phase velocity) and eigenfunction symmetry ("a" for antisymmetric and “s” for symmetric). Wall slip has contrasting effects on the two PDI families: it stabilizes PDI-1, whereas PDI-2 can be destabilized over a finite range of slip coefficients. This behavior reflects the different energy-transfer mechanisms of the two branches. PDI-1 is mainly sustained by energy extraction from the near-wall polymer-stress layer, while PDI-2 is governed more directly by shear-induced amplification of perturbation stresses. The polymer-diffusion term also contributes oppositely to the two branches, depending on the phase relation between the diffusive stress flux and the perturbation field. Direct numerical simulations confirm that perturbations of the same PDI type converge to similar nonlinear saturated states despite initial symmetry differences, validating the predictions of linear theory. PDI-2 modes show stronger wall localization in saturated states compared to PDI-1, which might arise from secondary instability, highlighting the role of boundary conditions in shaping nonlinear structures.

These findings enhance our understanding of viscoelastic flow stability under realistic slip conditions, offering a quantitative basis for controlling PDI in industrial applications like polymer processing. For polymer extrusion, regulating slip to stabilize PDI-2 can mitigate flow instabilities and reduce extrudate defects; in microfluidics, selective PDI manipulation via slip tuning may improve solution mixing efficiency. Future work should focus on experimental validation with diverse materials and extending analyses to models accounting for finite polymer extensibility, to improve real-system relevance.

ACKNOWLEDGMENTS

We would like to thank Rich Kerswell for helpful discussions on the polymer diffusive instability analysis. B.Z. and Z.D. are supported by the National Natural Science Foundation of China (Grant No. 52176065) and the National Natural Science Foundation of China (Grant No. 12102109). R.L. is supported by the National Natural Science Foundation of China (Grant No.12262008).

DATA AVAILABILITY

There are no publicly available research data or software supporting this manuscript. Requests for further information or data should be sent to the authors.

[1] R. Govindarajan and K. C. Sahu, Instabilities in viscosity-stratified flow, Annu. Rev. Fluid Mech. **46**, 331 (2014).

[2] S. S. Datta, A. M. Ardekani, P. E. Arratia, A. N. Beris, I. Bischofberger, G. H. McKinley, J. G. Eggers, J. E. López-Aguilar, S. M. Fielding, A. Frishman, M. D. Graham, J. S. Guasto, S. J. Haward, A. Q. Shen, S. Hormozi, A. Morozov, R. J. Poole, V. Shankar, E. Shaqfeh, H. Stark, V. Steinberg, G. Subramanian, and H. A. Stone, Perspectives on viscoelastic flow instabilities and elastic turbulence, Phys. Rev. Fluids **7**, 080701 (2022).

[3] R. Sureshkumar and A. N. Beris, Effect of artificial stress diffusivity on the stability of numerical calculations and the flow dynamics of time-dependent viscoelastic flows, J. Non-Newtonian Fluid Mech. **60**, 53 (1995).

[4] R. Sureshkumar, A. N. Beris, and R. A. Handler, Direct numerical simulation of the turbulent channel flow of a polymer solution, Phys. Fluids **9**, 743 (1997).

[5] J. Page, Y. Dubief, and R. R. Kerswell, Exact traveling wave solutions in viscoelastic channel flow, Phys. Rev. Lett. **125**, 154501 (2020).

[6] Y. Dubief, J. Page, R. R. Kerswell, V. E. Terrapon, and V. Steinberg, First coherent structure in elasto-inertial turbulence, Phys. Rev. Fluids **7**, 073301 (2022).

[7] S. Qin, M. Jiang, K. Ma, J. Su, and Z. Liu, Fully resolved simulations of viscoelastic suspensions by an efficient immersed boundary-lattice Boltzmann method, Particuology **75**, 26 (2023).

[8] T. Ohta, A. Hayashi, and S. Tsuzuki, A novel LES method for predicting drag reduction in viscoelastic fluid based on the time period of turbulence structures, J. Non-Newtonian Fluid Mech. **309**, 104924 (2022).

[9] M. Beneitez, J. Page, and R. R. Kerswell, Polymer diffusive instability leading to elastic turbulence in plane Couette flow, Phys. Rev. Fluids **8**, L101901 (2023).

[10] M. M. P. Couchman, M. Beneitez, J. Page, and R. R. Kerswell, Inertial enhancement of the polymer diffusive instability, J. Fluid Mech. **981**, A2 (2024).

[11] T. Lewy and R. Kerswell, The polymer diffusive instability in highly concentrated polymeric fluids, J. Non-Newtonian Fluid Mech. **326**, 105212 (2024).

[12] M. Beneitez, J. Page, Y. Dubief, and R. R. Kerswell, Transition route to elastic and elasto-inertial turbulence in polymer channel flows, Phys. Rev. Fluids **9**, 123302 (2024).

[13] M. Khalid, V. Shankar, and G. Subramanian, Continuous pathway between the elasto-inertial and elastic turbulent states in viscoelastic channel flow, Phys. Rev. Lett. **127**, 134502 (2021).

[14] P. Garg, I. Chaudhary, M. Khalid, V. Shankar, and G. Subramanian, Viscoelastic pipe flow is linearly unstable, Phys. Rev. Lett. **121**, 024502 (2018).

[15] M. Khalid, I. Chaudhary, P. Garg, V. Shankar, and G. Subramanian, The centre-mode instability of viscoelastic plane Poiseuille flow, J. Fluid Mech. **915**, A43 (2021).
[16] S. Pandey and V. Shankar, Effect of anisotropic mobility on the diffusive instability in viscoelastic shear flows, Phys. Rev. Fluids **10**, 053301 (2025).
[17] S. Ghosh, R. Usha, and K. C. Sahu, Linear stability analysis of miscible two-fluid flow in a channel with velocity slip at the walls, Phys. Fluids **26**, 014107 (2014).
[18] S. Ghosh, R. Usha, and K. C. Sahu, Double-diffusive two-fluid flow in a slippery channel: A linear stability analysis, Phys. Fluids **26**, 127101 (2014).
[19] G. Chattopadhyay, R. Usha, and K. C. Sahu, Core-annular miscible two-fluid flow in a slippery pipe: A stability analysis, Phys. Fluids **29**, 097106 (2017).
[20] M. EL Farragui, O. Souhar, and G. C. Georgiou, Newtonian annular Poiseuille and Couette flows with dynamic wall slip, Eur. J. Mech. B. Fluids **103**, 136 (2024).
[21] S. G. Hatzikiriakos, Wall slip of molten polymers, Prog. Polym. Sci. **37**, 624 (2012).
[22] M. D. Graham, The sharkskin instability of polymer melt flows, Chaos **9**, 154 (1999).
[23] Edited by S. G. Hatzikiriakos and K. B. Migler, *Polymer Processing Instabilities: Control and Understanding*, 1st ed. (CRC Press, Boca Raton, 2004).
[24] M. M. Denn, Extrusion instabilities and wall slip, Annu. Rev. Fluid Mech. **33**, 265 (2001).
[25] A. Abbasi Moud, J. Piette, M. Danesh, G. C. Georgiou, and S. G. Hatzikiriakos, Apparent slip in colloidal suspensions, J. Rheol. **66**, 79 (2022).
[26] G. C. Georgiou, On the stability of the shear flow of a viscoelastic fluid with slip along the fixed wall, Rheol. Acta **35**, 39 (1996).
[27] W. B. Black and M. D. Graham, Effect of wall slip on the stability of viscoelastic plane shear flow, Phys. Fluids **11**, 1749 (1999).
[28] M. Lellep, M. Linkmann, B. Eckhardt, and A. Morozov, Purely elastic linear instabilities in parallel shear flows with free-slip boundary conditions, J. Fluid Mech. **928**, R3 (2021).
[29] S. Pal and A. Samanta, Role of slip in the stability of viscoelastic liquid flow through a channel, Eur. J. Mech. B. Fluids **101**, 118 (2023).
[30] C. R. Doering, B. Eckhardt, and J. Schumacher, Failure of energy stability in Oldroyd-B fluids at arbitrarily low Reynolds numbers, J. Non-Newtonian Fluid Mech. **135**, 92 (2006).
[31] K. J. Burns, G. M. Vasil, J. S. Oishi, D. Lecoanet, and B. P. Brown, Dedalus: A flexible framework for numerical simulations with spectral methods, Phys. Rev. Res. **2**, 023068 (2020).
[32] D. Wang and S. J. Ruuth, Variable step-size implicit-explicit linear multistep methods for time-dependent partial differential equations, J. Comput. Math. **26**, 838 (2008).